

ARTICLE OPEN



Corrosion interactions between stainless steel and lead vanado-iodoapatite nuclear waste form part II

Tiankai Yao^{1,2,4}, Xiaolei Guo^{3,4}, Penghui Lei¹, Yachun Wang¹, Gerald S. Frankel³ and Jie Lian³✉

This paper studied the release of iodine from lead vanado-iodoapatite (I-APT, $\text{Pb}_{9.85}(\text{VO}_4)_6\text{I}_{1.7}$), a potential nuclear waste form for the radioactive waste element of I-129, which can be enhanced when crevice corrosion of stainless steel (SS) occurring nearby. Reference corrosion studies of I-APT were performed in different bulk solutions including DI water, 0.6 M and 6 M NaCl, and 0.1 M HNO_3 without metal crevice corrosion interactions. The localized enrichment of Cl^- , one of the major consequences of SS crevice corrosion, was found to be the decisive factor that led to the enhanced release of iodine. A surface alteration layer consisting of a mixture of nanocrystalline I-APT and Cl-rich apatite (Cl-APT) formed on I-APT surface. Meanwhile, large Cl-APT crystals formed at the crevice mouth on the I-APT surface. This study reveals a new near-field corrosion mechanism for ceramic waste forms when they are exposed to aggressive local corrosive conditions created by the electrochemical reactions of nearby metals. The insight gained in this study could be beneficial for a more accurate prediction of waste form degradation.

npj Materials Degradation (2020)4:15; <https://doi.org/10.1038/s41529-020-0119-9>

INTRODUCTION

Crystalline ceramics are important host materials for long-term immobilization of long-lived radioactive wastes such as actinides¹ and volatile iodine^{2,3}. The long-term stability of those crystalline ceramics can be verified by natural analogs that survive the million years of Earth's evolution⁴. Guided from nature, various materials systems have been developed as potential waste forms to immobilize the challenging radioactive wastes i.e., Synroc⁵ which contains the minerals of hollandite, zirconolite, and perovskite for various types of radionuclides, have been developed and proposed as potential waste forms to immobilize the challenging radioactive wastes. Apatite is a potential candidate for iodine immobilization⁶ due to its open channel along the z-axis of the hexagonal structure that can accommodate large-sized iodine atoms. Also, apatite shows remarkable thermal stability and exceptional resistance to iodine release in aqueous conditions^{7–9}, and calcium phosphate apatite is an earth-abundant mineral that shows exceptional stability to withstand natural weathering over millions of years. In addition, the apatite-structure type is also one of the major components of human bones and teeth in which materials should be durable against performance degradation and loss of functionality.

The aqueous corrosion of apatite under extreme conditions has been widely studied. More than eight models¹⁰, such as diffusion-controlled, polynuclear, etch-pit, and ion exchange, have been proposed to explain the corrosion process. However, due to the complexity of aqueous corrosion, none of these models can fully explain the experimental phenomena observed under different circumstances. In the presence of salts, such as Na_2SO_4 , NaCl, or sodium acetate, hydroxyapatite shows incongruent dissolution. The concentrations of dissolved Ca and P ions in solutions are proportional to salt concentrations, indicating that ion exchange is the dominant mechanism¹¹. Furthermore, one of the exclusive features for an ion-exchange governed aqueous corrosion process is the formation of a surface layer whose composition is different

than the parent phase¹⁰. It will be shown below that a similar surface film was also observed on corroded lead vanado-iodoapatite (I-APT, $\text{Pb}_{9.85}(\text{VO}_4)_6\text{I}_{1.7}$), therefore ion exchange was considered as the dominant corrosion mechanism of this material under the experimental conditions.

Crevice corrosion is a form of localized corrosion that is commonly observed on passive metals when they are partially shielded by other materials and corroded in aqueous environment containing aggressive anions such as Cl^- ions^{12,13}. Various types of corrosion resistant alloys, such as stainless steel (SS) 316^{14–18} and Alloy 22^{19–22}, have been considered to ensure the structural integrity of nuclear waste canisters. In general, crevice corrosion leads to the development of an aggressive environment in the confined crevice space, which may influence the durability of nearby materials. However, in conventional crevice corrosion studies, metals are usually pressed against chemically inert materials, such as polytetrafluoroethylene (PTFE) and durable ceramics²³. Therefore, the potential influence of metal crevice corrosion on adjacent non-metallic materials has not been well established. A recent account²⁴ has reported self-accelerated corrosion at the materials interface in which both glass and titanate-based ceramic waste forms display enhanced corrosion as a result of the variation of solution chemistry and acidity within a confined space of crevice corrosion, highlighting the importance of interactions at material interfaces in controlling the chemical durability and degradation behavior.

Part I of this paper reports the corrosion interactions between SS and a model ceramic waste form, lead vanado-iodoapatite (I-APT, $\text{Pb}_{9.85}(\text{VO}_4)_6\text{I}_{1.7}$), for the immobilization of radioactive iodine-129²⁵. It was found that the corrosion products of I-APT, including Pb-rich and V-rich species, are beneficial for the corrosion inhibition of SS. The inhibition mechanism can be attributed to the formation of surface films that inhibit the corrosion of the metal counterpart. However, this inhibition effect was limited with

¹Department of Mechanical Aerospace and Nuclear Engineering, Rensselaer Polytechnic Institute, Troy, NY 12180, USA. ²Materials and Fuel Complex, Idaho National Laboratory, Idaho Falls, ID 83402, USA. ³Department of Materials Science and Engineering, Ohio State University, Columbus, OH 43210, USA. ⁴These authors contributed equally: Tiankai Yao, Xiaolei Guo. ✉email: lianj@rpi.edu

the noticeable presence of the crevice corrosion characteristics observed on the SS surface.

In this Part II of the study, we report the influence of SS crevice corrosion on the release of iodine from I-APT and mechanistic understanding of the enhanced corrosion within a confined space with drastically altered solution chemistry and acidity. The results show that the localized corrosion of the ceramic waste form can be enhanced at crevice locations, forming a rim pattern with a high population of Cl-apatite precipitates. Benchmarking experiments using HNO₃ and different concentrations of NaCl as solvents indicate that the ion exchange between I of the I-APT and Cl⁻ in the solution is the governing mechanism for the aqueous corrosion of I-APT in the presence of a high concentration of negatively charged ions, such as Cl⁻, which are common anions in nuclear waste repository sites²⁶. The results presented in this paper underscore the possible occurrence of degraded iodine retention capability of I-APT waste form due to the initiation and proceeding of crevice corrosion from tight contact with canister metal alloys in the presence of Cl⁻ ions.

RESULTS

Formation and morphology of a band pattern on I-APT

The interaction experiments between SS and I-APT were conducted by pressing them against each other and corroding them in 0.6 M NaCl solution at 90 °C for 28 days. Since the SS and I-APT specimens were in direct contact with each other, and no external load was applied, the gap of the crevice was governed by the roughness of the samples. Optical profilometry analysis of the uncorroded SS and I-APT suggested an average roughness of less than 0.1 μm for both samples, therefore the gap of the SS and I-APT crevice should be on the submicron scale. The surface morphologies of the corroded I-APT specimens were examined by optical microscopy (OM) and scanning electron microscopy (SEM). Two groups of I-APT samples were studied, one in rectangular shape and one in round shape as shown in Fig. 1. Similar to the morphologies observed on SS as described in Part I, crevice corrosion characteristics²⁴ were identified on both I-APT samples, where corrosion damage was primarily localized at the boundary of the contact area (crevice mouth region). Both samples exhibited band patterns at the crevice mouth region with different contrast compared to the center of the samples. Similar patterns were observed on a model nuclear waste glass and a Cr-bearing hollandite waste form sample²⁴, both of which were corroded in close proximity to SS under similar conditions. This suggests that the observed morphologies are directly associated with SS crevice corrosion. It is worth-noting that the morphologies on the two I-APT specimens were slightly different with respect to the

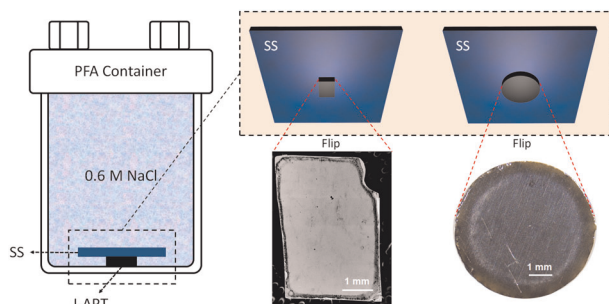


Fig. 1 Stainless-steel and iodoapatite corrosion interaction. Schematic illustration of the experimental setup for SS and I-APT corrosion and the surface morphologies of two groups of I-APT samples, one rectangular and one round shape, corroded in close proximity to SS in 0.6 M NaCl solution for 28 days. The image of the rectangular sample was taken by SEM and the image of the round sample by OM.

formation of secondary phases and the pattern of a surface alteration layer. Specifically, an appreciable amount of secondary phases formed in the crevice mouth area of the rectangular sample, which exhibited a dark band pattern as shown in Fig. 1. In contrast, no second phases were visible on the surface of the round-shaped sample. Instead, corrosion products with brown color were deposited at the crevice mouth region. The difference may be associated with the different gap size of the crevice, and the different sample geometry that may affect the distance for diffusion of ion species. Both factors could influence the mass transport inside the crevice, and eventually the corrosion morphologies. More interpretations are given in the discussion section.

To better understand the formation mechanism of the band pattern, the rectangular-shaped I-APT sample corroded in close proximity to SS in 0.6 M NaCl solution for 28 days at 90 °C was cross-sectioned and the microstructure/morphology were observed by SEM and energy dispersive spectroscopy (EDS). The change of elemental distribution directly underneath the band pattern formed on I-APT (Fig. 2) was examined. The top surface of the cross-section in Figs. 2a, b was in direct contact with SS during the corrosion experiment. The bottom surface was in contact with perfluoroalkoxy alkane (PFA) containers; while the left and right surfaces were immersed directly in bulk solution. The area highlighted in the orange box was directly underneath the band pattern presented in Fig. 1. As shown in the EDS elemental map (Fig. 2c), a zone depleted of iodine and enriched in chlorine was observed in the outermost layer of the corroded I-APT. This observation supports the hypothesis that ion exchange between I from I-APT and Cl⁻ ions from the leaching solution is the dominant corrosion mechanism of I-APT. In contrast, Pb and V were distributed uniformly across the region.

Elementary distribution across the interface

Upon closer examination, it is evident that the depletion of I was locally enhanced at the crevice mouth. The typical depth of I depletion layer was about 30 μm on the I-APT surface that was in direct contact with SS (top surface). However, in the crevice mouth region, the thickness of the alteration layer reached approximately 200 μm. The width of this leaching zone was about 80 μm, which roughly matched the width of the band patterns existing at the crevice mouth of I-APT. It could be argued that the increased thickness of the alteration layer in this area may be due to the exposure of I-APT to the NaCl bulk solution, which has a higher surface area to solution volume (S/V) ratio. However, as shown in Fig. 2c, the thickness of the alteration layer formed on the edge exposed to the bulk solution was only about 15 μm, which is much smaller than that observed in the crevice mouth region. It is also possible that the enhanced alteration layer thickness was caused by an edge effect due to a higher amount of surface defects. However, the enhanced leaching effect was not observed in the crevice mouth area of I-APT and the PFA container (Fig. 3). The S/V ratios are similar for both sides, so the corrosion behavior on the bottom surface in contact with PFA could serve as a good reference. As shown in Fig. 3c, the alteration layer thickness on the back side (surface facing the PFA container) of the I-APT was typically 20–30 μm, which was similar to that of the surface in contact with SS. This thickness was uniform throughout the entire surface on the bottom side, suggesting the absence of the effect of localized corrosion present on the top surface. Comparing the different alteration layer thicknesses in the two crevice mouth regions, it could be concluded that the release of I from I-APT was influenced by the crevice corrosion of nearby SS.

The cross-sectional area shown in Fig. 2a was further investigated by electron probe micro-analysis (EPMA), providing more accurate quantitative analysis of elemental concentrations across the examined area (Fig. 4). An iodine map based on EPMA

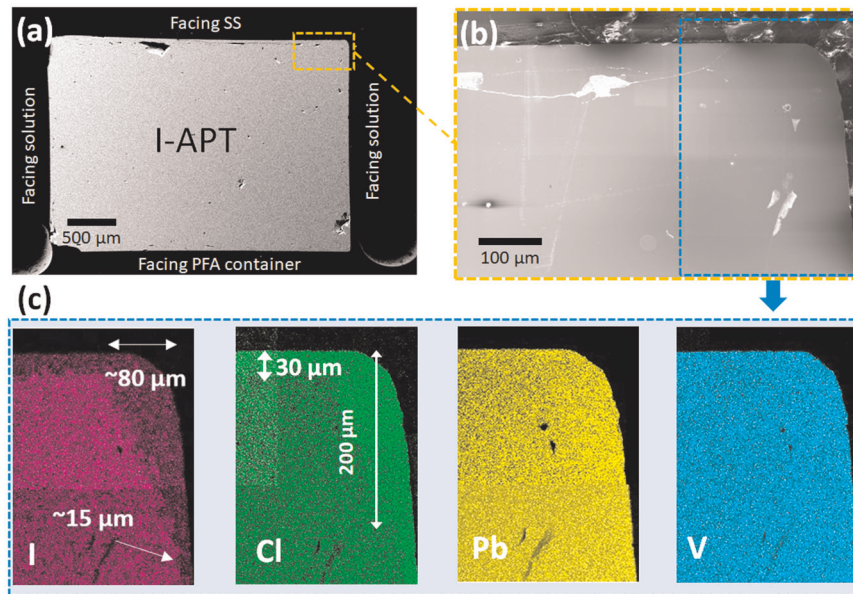


Fig. 2 Characterization of cross-section of a rectangular I-APT sample corroded in close proximity to SS in 0.6 M NaCl solution for 28 days. **a** A SEM image of the entire cross-section. **b** A SEM image of a selected area right underneath the SS/I-APT crevice mouth area. **c** EDS elemental maps of the selected area as indicated in the blue box. **b**, **c** Share the same scale bar. Each elemental map was stitched by two separate images.

results is inserted within a backscattered electron (BSE) image of the corresponding area. The presence of iodine in the alteration layer was recognizable based on the contrast even though it was significantly depleted in this region. A line scan based on EPMA was also conducted from the outermost surface to the pristine I-APT matrix as indicated by the pink line shown in Fig. 4a. The concentration profile of the four major elements (Pb, V, I, and O) were acquired (Fig. 4b), which showed a gradual increase of iodine concentration from zero to 4.2% along the 30 μm thick alteration layer. The saturated concentration was consistent with the theoretical value of 4.1% based on the chemical composition of $\text{Pb}_{9.85}(\text{VO}_4)_6\text{I}_{1.7}$, indicating the EPMA line scanning covered the entire corrosion layer. The other three elements, including Pb, V, and O, showed much less variation across the examined surface layer, except for the outermost 3 μm , which could possibly be the gap between sample and epoxy mount.

Formation of Cl-APT crystals and alteration layer

Besides the formation of a surface alteration layer on I-APT, an appreciable amount of crystals were visible on the surface of the corroded I-APT sample, primarily located in the SS/I-APT crevice mouth region (Figs. 5a, b). As shown in Fig. 5c, SEM-EDS analysis indicates that the major elements of the crystals were Pb, V, O, and Cl, suggesting the presence of Cl-APT. To provide direct crystal structure information, a transmission electron microscopy (TEM) sample (Figs. 5d, e) was prepared from the region of the surface alteration layer with crystals by a focused ion beam lift-out technique. The crystals were found to be single-phase and the two sets of electron diffraction patterns shown in Fig. 5g, h were indexed as the [110] and [131] zone axes of a hexagonal phase, respectively. Combined with EDS results, these large crystals can be determined to be $\text{Pb}_5(\text{VO}_4)_3\text{Cl}$.

The alteration layer underneath the crystals showed a nanocrystalline feature (Figs. 5i, j). There were intergranular tunnels inside the layer, potentially serving as the shortcut for mass transport between the pristine phase and solution during the corrosion process. The selected area electron diffraction pattern in Fig. 5k showed a feature of rings with various distances, which can be well indexed to an apatite structure with a hexagonal crystal

symmetry. Given that this layer was enriched in Cl and depleted in I based on the SEM-EDS analysis, it is reasonable to speculate that the alteration layer was either a solid mixture of two apatite phases, i.e., Cl-APT and I-APT, or a solid solution of Cl-I-APT formed by the partial replacement of I with Cl. However, the resolution of diffraction pattern did not allow unambiguous determination of these two phases due to similar lattice parameters.

In this work, two different shapes of I-APT samples were studied. The rectangular-shaped I-APT showed a thicker surface alteration layer at the crevice mouth, as demonstrated in Figs. 2–4. The enhanced alteration layer thickness suggested the influences of SS crevice corrosion. A similar phenomenon was observed for the round-shaped samples. However, the effect of SS crevice corrosion on these round-shaped samples seemed to be much more substantial (Fig. 6). It should be noted that the cross-section of the rectangular shaped I-APT as shown in the Figs. 2–4 was abraded to 1200 grit before characterization, but the cross-sections of the round shaped samples were directly subjected to observations without any surface preparation. This may partially explain the distinct surface morphologies observed on the two samples. The cross-sections of the round-shaped I-APT after 7 and 28 days of corrosion were examined by OM and the results are presented in Figs. 6a, b, respectively. An I-APT sample corroded in close proximity to PTFE was also examined as a control sample (Fig. 6c). For all three samples, the top and bottom surfaces were in contact with SS/PTFE and PFA containers, respectively; while the left and right sides were exposed to the bulk solution. The cross-sections were further characterized by SEM in Figs. 6d, e, and a time dependent corrosion pathway can be observed. The localized corrosion in the SS/I-APT crevice mouth area created a thick layer on I-APT (region 1, outlined by the red dashed line in Fig. 6d) after only 7 days of corrosion. Similar to what was observed in Fig. 2, the thickness of the alteration layer was the largest in the SS/I-APT crevice mouth region. Additionally, no an apparent alteration layer was found in the I-APT/PFA crevice mouth area. After 28 days of corrosion, the thickness of the alteration layer increased drastically compared to that of 7 days, which exceeded 1 mm at several locations. A clearly-resolved core-shell structure formed, where the pristine phase was preserved in the core and surrounded by a thick shell layer as

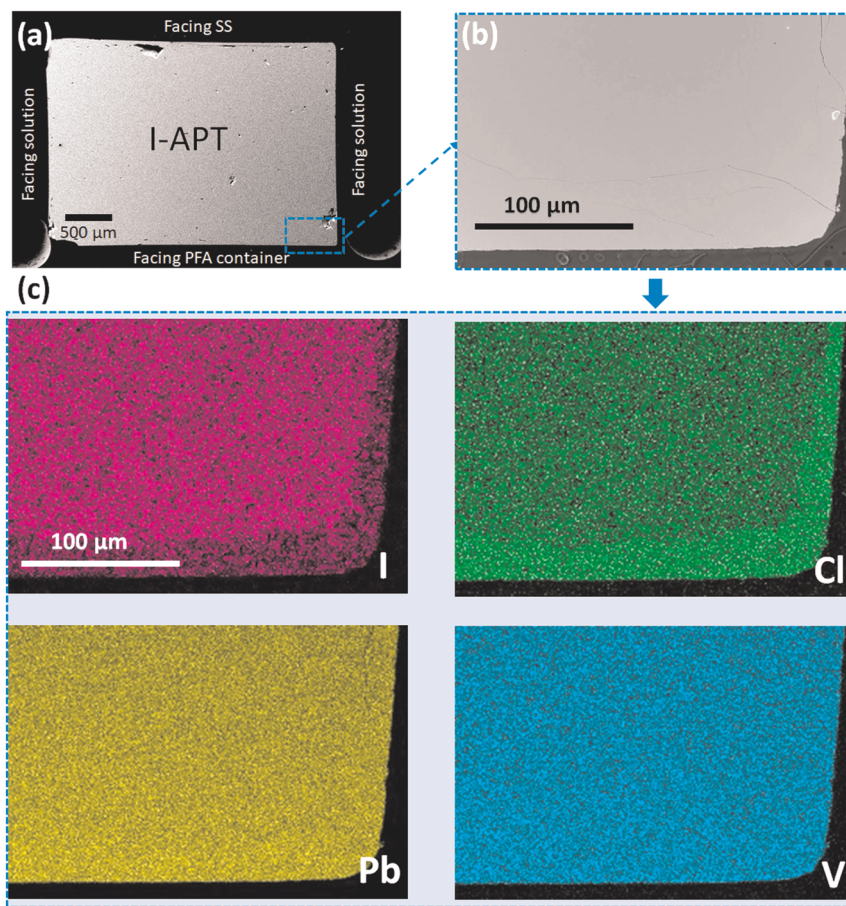


Fig. 3 Characterization of cross-section of a rectangular I-APT sample in close proximity to PFA in 0.6 M NaCl for 28 days. **a** A SEM image of the entire cross-section. **b** A SEM image of a selected area right above the I-APT/PFA crevice mouth area. **c** EDS elemental maps of a selected area as indicated in the blue box. **b, c** Share the same scale bar.

outlined by the red dashed lines in Fig. 6e. Comparing the corrosion morphologies shown in Figs. 6d, e, it could be hypothesized that the corrosion of I-APT was initially dominant in the SS/I-APT crevice mouth area, and was likely affected by SS crevice corrosion. Following the alteration of the outermost surface layer, the corrosion front moved gradually into the pristine phase over time, which led to the formation of the observed microstructures shown in Fig. 6e. On the other hand, the I-APT sample corroded near PTFE (Figs. 6c, f) did not show distinctively enhanced localized corrosion features as observed in Fig. 6e after 28 days of immersion. The difference between Figs. 6e, f indicates that I-APT corrosion was strongly enhanced by the crevice corrosion of SS.

The corroded and uncorroded I-APT samples were further characterized by X-ray powder diffraction (XRD) (Fig. 6d), which showed a gradual replacement of I-APT by Cl-APT during corrosion. The locations and relative intensities of the theoretical peaks for I-APT and Cl-APT are also included as references. Both I-APT and Cl-APT have a hexagonal crystal structure, but I-APT has a slightly larger lattice constant due to the large ionic radius of iodine. Therefore, I-APT and Cl-APT have similar XRD spectra with a slight shift in peak positions. The positions of the X-ray diffraction peaks from pristine I-APT matched well with the theoretical values. However, the spectra of the corroded I-APT gradually deviated from pristine I-APT and approached that of Cl-APT, which became more evident for the I-APT corroded after 28 days compared to that of the 7 days. However, the x-ray diffraction peaks for I-APT were still recognizable after 28 days of corrosion, although the intensity was much lower than that of Cl-APT. These results are

consistent with the EDS data shown in Fig. 2, which showed the presence of both iodine and chlorine in the alteration layer, although the concentration of the former was much lower. It is also worth noting that the structure disorder of the alteration layer on I-APT seemed to increase over corrosion time. With the diminishing of intensity due to corrosion, the peaks for I-APT were less resolved compared to those in the pristine phase. Instead, these peaks overlapped each other, forming big shoulders at two-theta angles of 28.5 and 29.5 degrees. This could be attributed to the partial replacement of I^- by Cl^- in I-APT, which changed the local crystal structure.

Raman spectroscopy was also used to characterize the I-APT samples because it provides complementary information about the studied crystal structure from a bonding perspective. The Raman spectra are relatively well established for apatite structures. On the presented range from 600 to 1000 cm^{-1} , the major bonding information is the stretching vibration mode of VO_4 tetrahedra²⁷. The replacement of I^- by Cl^- may change the bonding environment of VO_4 , yielding a peak around 787 cm^{-1} . The spectra were acquired from four different samples, including pristine I-APT, pristine Cl-APT, cross-sections of I-APT samples after 28 days of corrosion with SS and PTFE, respectively. For the latter two groups of samples, two locations were examined, the center of the cross-section and the outermost surface layer, as indicated in Figs. 6e, f. The core-shell structure of I-APT corroded near SS was relatively easy to distinguish. Although the core-shell structure did not exist on I-APT corroded near PTFE, similar locations designated as “center” and “edge” were investigated. The results are shown in Fig. 6e. The core of I-APT corroded near

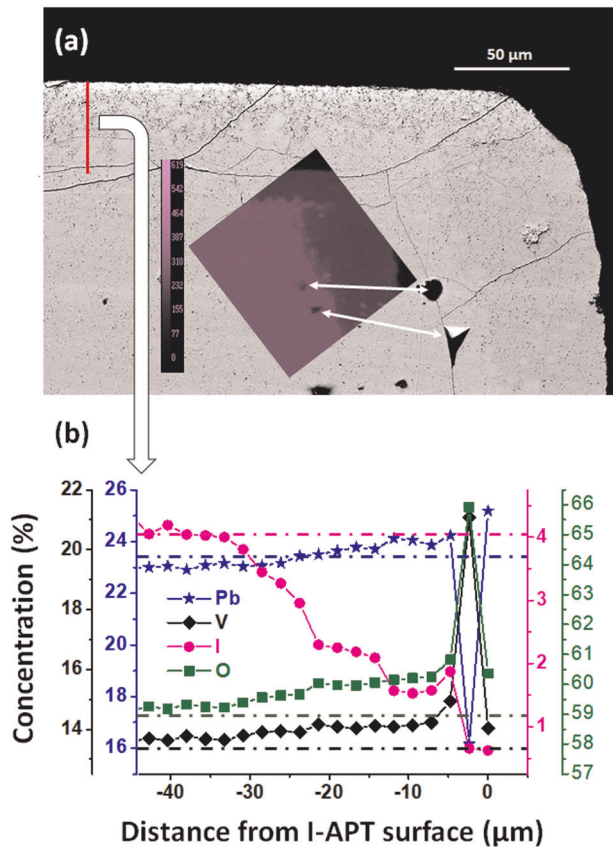


Fig. 4 Microstructure and microchemistry characterization of the cross-section of a rectangular I-APT sample corroded in close proximity to SS in 0.6 M NaCl solution for 28 days. **a** A BSE image of I-APT from the same area as shown in Fig. 2b. An EPMA elemental map of iodine was inserted. The dark spots as indicated by the white arrows are defects on the sample, probably induced during sample preparation. **b** A line scan of different elements based on EPMA results along the ~30-micron surface alteration layer as indicated by the red arrow shown in **a**.

SS shared the same spectra as the pristine I-APT, indicating that this part was not corroded. On the other hand, the shell of the I-APT corroded near SS showed similar spectra with pristine CI-APT, but the peak positions slightly varied. This again indicates incomplete displacement of I^- with Cl^- in this region, which is in line with the XRD and EDS results. In contrast, the Raman spectra of the I-APT corroded near PTFE were almost identical for the center and edge regions, suggesting no alteration in the edge region. This further validates the significant enhancement of I-APT corrosion by the nearby crevice corrosion of SS.

DISCUSSION

Typical crevice corrosion in Cl^- containing solutions results in the formation of an aggressive environment in the confined crevice region, including enrichment in H^+ and Cl^- ions¹². To better understand the roles of these aggressive species on the corrosion of nearby I-APT, reference corrosion tests were conducted by the immersion of I-APT samples in different solutions: DI water, 0.6 M NaCl, 6 M NaCl, and 0.1 M HNO_3 at 90 °C for 28 days. All I-APT samples were corroded without the presence of a SS crevice. To provide enough nucleation sites for apatite crystals, one sample was intentionally roughened to 600 grit prior to immersion in 6 M NaCl solution. The major results of I-APT corrosion in different NaCl concentrations, including iodine release, degradation mechanisms, alteration layer formation, and microstructure evolution,

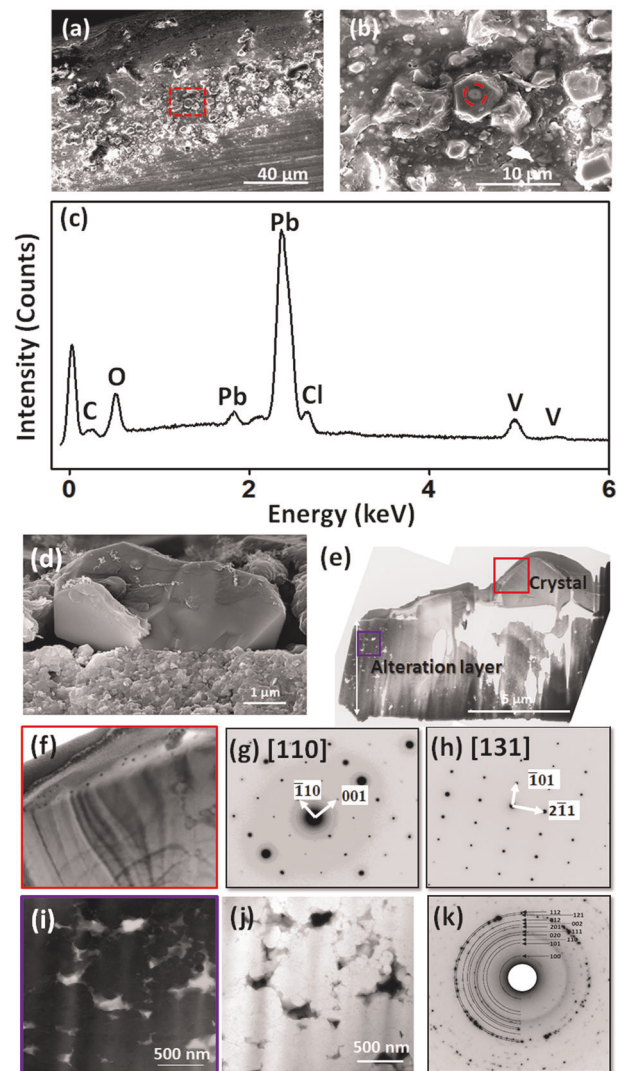


Fig. 5 Microstructure characterization of the secondary phase particles precipitated on I-APT surface in the crevice mouth area and the surface alteration layer of I-APT. **a** A SEM image of surface morphology of I-APT in the crevice mouth area (i.e., the band pattern shown in Fig. 1); **b** A close-up view of a selected area as indicated in **a**, where large secondary phase crystals are observed; **c** EDS point analysis conducted on a location as indicated by the red circle in **b**; **d**, **e** A lift-out foil prepared by focused ion beam, which contains a large crystal as shown in **b**; **f** A TEM image collected on the crystal from an area as indicated by the red box in **e**; and **g**, **h** Selected area diffraction patterns along two different zone axes, which were acquired from the area shown in **f**. The surface alteration layer on I-APT exhibited nano-crystalline features as shown in the **i** a bright-field TEM image and **j** a dark-field TEM images; and **k** Electron diffraction ring patterns collected from the alteration layer of I-APT.

were reported in a separate paper²⁸. Here, we briefly discuss the morphology variation and secondary phase formation in the chloride solutions as benchmarking experiments, which are useful for comparison with the behavior of the I-APT upon interaction with SS with drastically changed solution chemistry, specifically high Cl^- concentrations, in the confined crevice.

Needle-shaped secondary phases (Fig. 7a) were observed on the I-APT surface after 28 days of corrosion testing in DI water. The crystal morphology was different from that observed in Fig. 5. The crystals were similar to the hydroxyapatite synthesized by a solution-based reaction at ~100 °C²⁹. For I-APT corroded in 0.6 M

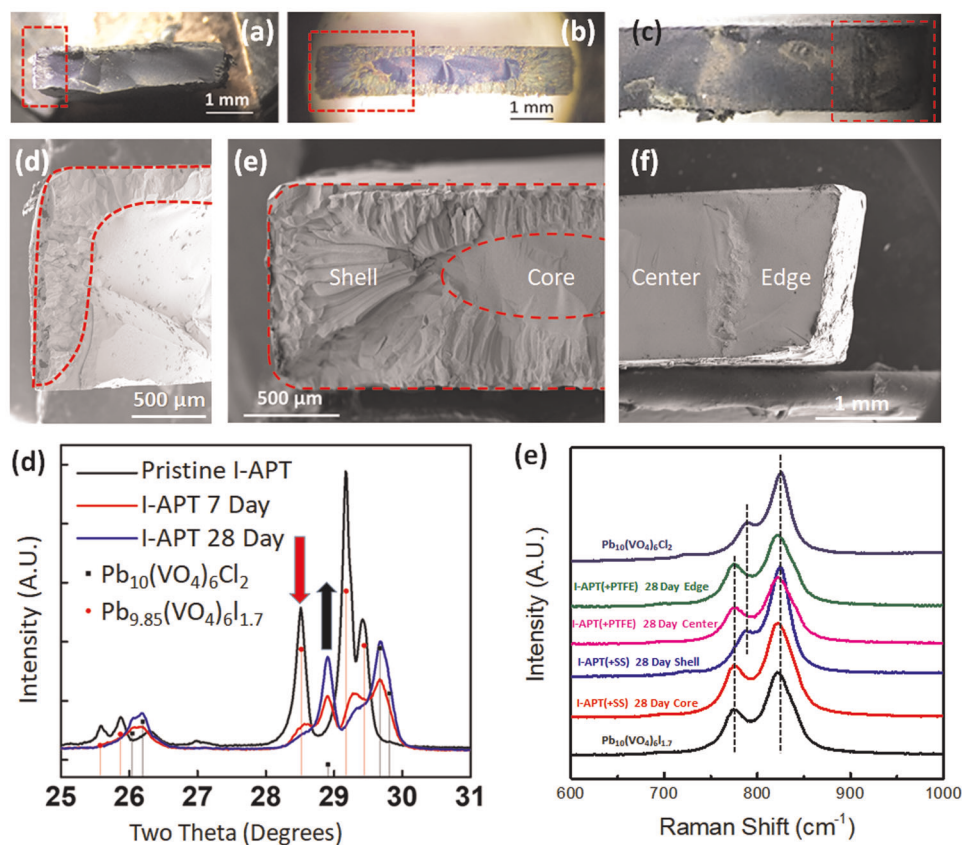


Fig. 6 Characterizations of cross-sections of round-shaped I-APT samples corroded in close proximity to SS or PTFE in 0.6 M NaCl solution at 90 °C. **a–c** Optical microscopy images and **d–f** SEM images that were collected from areas indicated in the red box in **a–c**. **a, d** Cross-sections of I-APT corroded near SS for 7 days. Areas with a clearly visible alteration layer are outlined in red dash lines. **b, e** Cross-sections of I-APT corroded near SS for 28 days. Areas with a clearly visible alteration layer are outlined in red dashed lines. **c, f** Cross-sections of I-APT corroded near PTFE after 28 days. For all the three samples, the top and bottom surfaces were in contact with SS/PTFE and PFA containers, respectively; while the left and right sides were exposed to the bulk solution. XRD (**d**) and Raman (**e**) spectra show the gradual replacement of I-APT by Cl-APT proportional to experimental duration.

NaCl solution, no large crystals formed on the sample surface (Fig. 7b). By increasing the NaCl concentration to 6 M in the benchmarking experiments, large crystals appeared on the I-APT surface, with similar morphologies as those observed in the I-APT/SS crevice mouth region. These comparisons clearly indicate that a high concentration of Cl^- ions (>0.6 M) may exist in the I-APT/SS crevice mouth area during the crevice corrosion of SS. Surface roughness also played a key role in the formation of secondary phases. The I-APT sample purposely roughened to 600 grit and corroded in 6 M NaCl showed a much higher population of crystals (Fig. 7d), similar to the regions inside the band pattern on I-APT after 28 days corrosion with SS (Fig. 5b). This could be attributed to the surface defects introduced to the I-APT surface by grinding, which served as nucleation sites for the precipitation of Cl-APT.

On the other hand, after 7 days of corrosion in 0.1 M HNO_3 solution (pH = 1), the I-APT structure dissolved completely, accompanied by the formation of new crystals with cuboidal morphologies (Fig. 7e). Raman spectra collected from these crystals indicated a chervetite structure, $\text{Pb}_2\text{V}_2\text{O}_7$ (Fig. 7f). The Raman spectra were significantly different compared to those collected from the precipitated phases on SS surface corroded near I-APT (see Part I²⁵). As a matter of fact, the formation of chervetite may be more favorable than apatite under acidic conditions. Previous studies have shown that the presence of acids during wet chemical synthesis led to the formation of chervetite rather than apatite⁶. These results indicate that the precipitation of crystals shown in Figs. 5a, b may be primarily

influenced by the enrichment of Cl^- ions at the crevice mouth instead of H^+ ions. The absence of chervetite phase on the I-APT surface corroded near SS also suggests that the local pH may be higher than 1. However, in a typical SS crevice, the local pH could be lower than 1¹². This indicates that the crevice corrosion of SS may have been locally suppressed by the corrosion products of I-APT, which is consistent with the results presented in Part I of this paper²⁵.

One interesting observation was the different corrosion morphologies present on the rectangular and round shaped samples. As shown in Fig. 1, the band of damage was about 0.2 mm from the edge for the rectangular shaped sample, which appeared to be smaller than that of the round shaped sample (~0.7 mm). In this specific region, the mass transport rate was the most rapid, but the ohmic potential drop was also the lowest. The location of the observed band was likely determined by the interplay between the two factors, which was fundamentally governed by the geometry of the crevice including the crevice gap and the size of the contact area. The gap of the crevice should be similar for the two groups because the samples were all ground to similar surface finishes. However, mass transport in crevice corrosion is dominated by the smallest gap of the crevice rather than the average gap, which could introduce uncertainties to the crevice systems under comparison. The crevice area for the round-shaped I-APT was approximately 29.2 mm², which was larger than that of the rectangular one (14.6 mm²). The larger crevice area may increase the mass transport limitation inside the crevice and thus enhance the enrichment of Cl^- ions. Meanwhile, all the SS

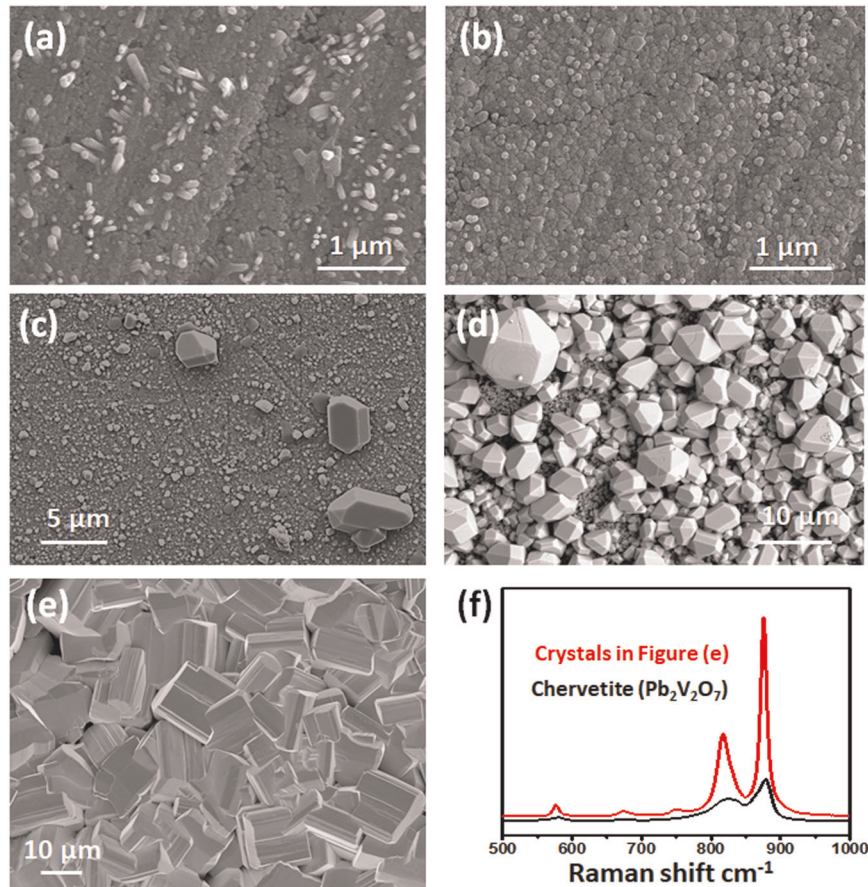


Fig. 7 Surface corrosion products on I-APT samples corroded in various aqueous conditions. SEM images showing sample surface morphologies in **a** DI water **b** 0.6 M NaCl **c** 6 M NaCl, and **d** 6 M NaCl with coarsened surface, **e** pH = 1 solution, and Raman spectrum (**f**) for the crystals in **e**, indicating the crystal formed is $\text{Pb}_2\text{V}_2\text{O}_7$ chervetite.

specimens used in this study were of the same size. The total SS area was over 40 times larger than the contact area of SS and I-APT. Additionally, the solutions were all aerated, so the corrosion was likely under anodic control. Therefore, although the exterior to interior area ratios were different for the two groups of samples, the difference may not have a significant influence on the crevice corrosion studied here. The different crevice geometry may also explain the different thickness of the alteration layers observed on the round shaped I-APT sample (Fig. 6) and the rectangular shaped sample (Figs. 2–3) exposed for the same period of time. Apparently, the mass transport limitation was greater for the round-shaped sample due to the larger crevice depth, which induced a greater ohmic potential drop between the crevice mouth and crevice center compared to the rectangular sample. This larger ohmic potential drop could also shift the potential of the anodic site to the active region and subsequently assist the propagation of the crevice corrosion^{30,31}, thereby enhancing the corrosion of I-APT.

Based on all observations, a crevice corrosion mechanism is proposed and schematically illustrated in Fig. 8. When SS is partially shielded from the solution by I-APT, a confined crevice space forms at the interface of the two materials. When the materials are exposed to solution containing aggressive anions that can break down the passivity of SS, such as Cl^- ions, crevice corrosion of SS occurs. Metal cations including Fe^{2+} , Cr^{3+} , and Ni^{2+} are released into the crevice solution by anodic dissolution of SS. These cations then hydrolyze and form a high concentration of H^+ that acidify the local solution. The V-rich and Pb-rich corrosion products of I-APT may suppress the dissolution kinetics of SS, making the local environment less aggressive, but these species

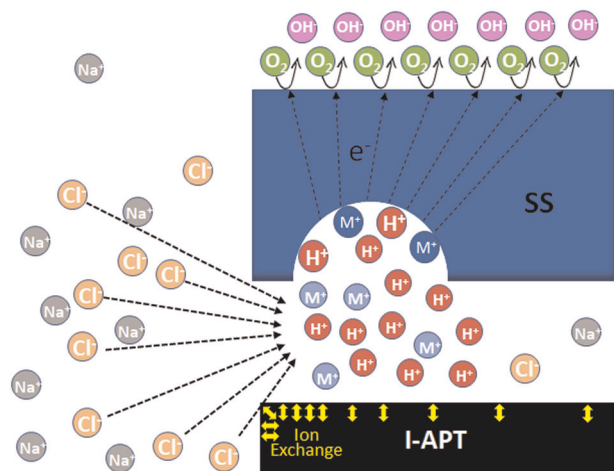


Fig. 8 Crevice corrosion and metal-ceramic interaction. A schematic illustration of corrosion mechanism of SS and I-APT in NaCl solution.

do not manage to completely shut down the reactions. The anodic dissolution is always accompanied by cathodic reactions, which is the oxygen reduction reaction under the experimental conditions. Due to the mass transport limitation inside the confined crevice space, the local oxygen is quickly consumed and cannot be replenished at a sufficient rate. Therefore, the cathodes move to the outside of the crevice, where more oxygen is accessible. The

separation of anode and cathode continues to drive the enrichment of metal cations and H^+ inside the crevice. Owing to their high mobility, Cl^- ions in the bulk solution migrate into the crevice to balance the charge inside the crevice. During this Cl^- migration process, the kinetics of ion exchange between Cl^- ions from the solution and I^- ions from the I-APT substrate may be increased, which explained the larger alteration layer thickness of I-APT, especially at the SS/I-APT crevice mouth region. In this particular region, the ohmic potential drop between the anode and cathode is low, so the anodic corrosion rate is usually high. This leads to the formation of a highly reactive zone at the crevice mouth, which in turn affects the corrosion rate of I-APT that is present nearby. It has been known that the release rate of iodine from I-APT depends on the salt concentration³². Therefore, the increased alteration layer thickness on I-APT, along with the precipitation of large crystals in the SS/I-APT crevice mouth area, can be well explained by this mechanism.

It has been well documented that apatite is a durable waste form for the immobilization of iodine^{2,8,33}. In neutral solutions with low ionic strength, a typical environment for underground water^{34,35}, the release rate of I^- is very low³³. This has also been verified in Figs. 6c, f, which did not show the presence of visible alteration layer when I-APT was corroded in close proximity to PTFE in solutions even with a much higher ionic strength (0.6 M NaCl) than the possible ground water environment. Additionally, the precipitation of large crystals was not observed when I-APT was exposed to 0.6 M NaCl bulk solution under similar experimental conditions. This indicates the high chemical durability of I-APT itself as a nuclear waste form proposed for the immobilization of long-lived radioiodine if SS crevice corrosion is absent. However, when I-APT was corroded in close proximity to SS, the release rate of I^- was accelerated, particularly near the crevice mouth region. Therefore, this study revealed a new corrosion mechanism when I-APT waste form is encapsulated in metallic canisters and exposed to a Cl^- enriched aqueous environment. The actual ground water chemistry of the deep geological repository is certainly much more complicated than 0.6 M NaCl, and will vary with specific repository sites. However, it will contain Cl^- ions, although at very low concentration (several mM)^{26,34}. Although the initial concentration of the Cl^- ions may be lower than 0.6 M, it could be enriched in the confined space due to electro-migration during the localized corrosion of metallic canisters¹². Therefore, this study is important for the deployment of I-APT as a ceramic host for I-129. When designing new waste forms for the immobilization of problematic radionuclides, their potential corrosion interactions with the metallic canisters might be taken into account. In addition to the high acidity reported in a previous study²⁴, the influence of halide ions enrichment could also play a critical role in the near-field corrosion of the nuclear waste packages.

Although the present study was conducted in a simulated oxic environment relevant to the U.S. Yucca Mountain project, it also has implications for the anoxic environment expected in repositories proposed by many other countries. These repositories will be constructed in the saturated zone, where no oxygen is expected. However, other oxidants could still exist in such environment. For instance, Glass et al.¹⁴ have demonstrated that gamma-radiation, which could be generated by the immobilized radionuclides, could induce the formation of the strong oxidants H_2O_2 and $\cdot OH$. It was found that these oxidizing species could shift the potential of stainless steel toward anodic direction by 150–250 mV, which may cause the open circuit potential to exceed the crevice corrosion repassivation potential and thus trigger crevice corrosion in anoxic conditions. Similar conclusions have been made by Worthington et al., who suggested that gamma-radiation promoted not only the initiation, but also the propagation of crevice corrosion in deaerated conditions³⁶. Therefore, the development of a total system performance

assessment of a repository that utilized accurate predictions of all of the relevant processes could improve repository designs. In such a case, the near-field corrosion interaction described in this study would be important and beneficial.

In summary, this paper describes the potential corrosion interactions between a potential ceramic nuclear waste form, I-APT, and a candidate canister alloy, SS, in 0.6 M NaCl at 90 °C. The I-APT sample was systematically analyzed with SEM, EDS, EPMA, XRD, and TEM. The results show that the presence of SS crevice corrosion accelerates the alteration of I-APT, which is accompanied by the enhanced release of iodine from the outermost surface layer and the formation of Cl-contained APT fine particles, as well as the precipitation of large Cl-APT crystals in the SS/I-APT crevice mouth area. Through benchmarking studies of pure I-APT corroded in DI water, NaCl mediated solutions and 0.1 M HNO_3 , the corrosion mechanism of I-APT in crevice corrosion configuration is determined to follow ion exchange and surface reprecipitation. The processes are similar to I-APT corroded in bulk solutions without crevice corrosion. However, the corrosion rate is accelerated due to the enrichment of Cl^- ions in the SS/I-APT crevice mouth area associated with SS crevice corrosion.

METHODS

Sample preparation

The I-APT was synthesized through high energy ball milling of constituent iodine and oxide and densified into dense pellets form by spark plasma sintering, which has been reported elsewhere². The pellet surface was ground with different grades of sandpaper and finished by 1 μm diamond lapping films. The surface of SS 316 (~25.4 mm \times 25.4 mm \times 3 mm) was abraded to 1200 grit with SiC papers and washed in DI water and ethanol. Both I-APT and SS specimens were dried thoroughly before usage. Additional I-APT samples were also prepared for reference corrosion tests without the presence of SS. The majority of these I-APT samples were abraded in the same way as those used for crevice corrosion, however, one of those samples was purposely roughened by an additional grinding by a 600 grit SiC paper on the polished surface.

Crevice corrosion experiment

The corrosion interaction experiment setup is shown in Fig. 1. The I-APT and SS specimens were pressed against each other and wrapped with Teflon tape to secure their positions during the exposure. Two groups of I-APT samples were used: one group with a rectangular shape (~3.1 mm \times 4.7 mm \times 0.2 mm) and the other with a round shape (diameter ~6.1 mm). The whole structure was immersed in a 0.6 M NaCl solution at 90 °C in PFA containers. The temperature of 90 °C is commonly used for accelerated laboratory testing for waste form performance assessment^{37–39}. Since crevice corrosion of SS316 can still occur at room temperature¹³, the mechanism proposed here is likely valid. The corroded samples were collected after 7 and 28 days of exposure. Reference corrosion experiments were conducted by immersing I-APT samples in different solutions in PTFE containers at 90 °C without the presence of SS. The testing solutions included DI water, 0.6 M NaCl, and 6 M NaCl, and 0.1 M HNO_3 solutions.

Microstructure characterization

Microstructure characterization was conducted using a Carl Zeiss Supra 55 (Jana, Germany) field emission SEM. TEM samples were prepared using the focused ion beam method in an FEI Versa 3D dual beam system. TEM analysis was conducted in a JOEL 2011. Electron-probe microanalysis (EPMA) was conducted in a Cameca SX-100 system. X-ray diffractions of the sintered pellets were acquired by a Panalytical X'Pert XRD system (Westborough, MA, USA) using Cu Ka ($\lambda = 1.5406 \text{ \AA}$) irradiation. Before each run, the X-ray beam was aligned with a direct beam through a 0.2 Cu beam attenuator, and further calibrated by scanning on a standard Al_2O_3 sample. The sample height was aligned with the X-ray beam bisected. A scanning step of 0.013° with 2 seconds per step was adopted. Micro-Raman spectra were collected at room temperature through a Renishaw Micro-Raman spectrometer equipped with an argon-ion laser (514.5 nm). A typical spectrum was acquired with an exposure time of 10 s and 10 accumulations under an operation power of 20 mW. An extended scanning region from 600 to 1000 cm^{-1} was chosen since it contains characteristic peaks

for apatite structure. The laser power was fixed at 100% because lower laser power yielded similar spectra but lower signal to background ratios.

DATA AVAILABILITY

The data that support the findings of this study are available from the corresponding author upon request.

Received: 5 February 2020; Accepted: 29 April 2020;

Published online: 04 June 2020

REFERENCES

- Ewing, R. C., Weber, W. J. & Lian, J. Nuclear waste disposal-pyrochlore (A₂B₂O₇): nuclear waste form for the immobilization of plutonium and “minor” actinides. *J. Appl. Phys.* **95**, 5949–5971 (2004).
- Yao, T., Scott, S., Xin, G., Lu, F. & Lian, J. Dense iodoapatite ceramics consolidated by low-temperature spark plasma sintering. *J. Am. Ceram. Soc.* **98**, 3733–3739 (2015).
- Campayo, L., Le Gallet, S., Perret, D., Courtois, E., Cau Dit Coumes, C. et al. Relevance of the choice of spark plasma sintering parameters in obtaining a suitable microstructure for iodine-bearing apatite designed for the conditioning of I-129. *J. Nucl. Mater.* <https://doi.org/10.1016/j.jnucmat.2014.10.026> (2015).
- Lumpkin, G. R. & Geisler-Wierwille, T. *Comprehensive Nuclear Materials* 563–600 (Elsevier, 2012).
- Smith, K. L., Lumpkin, G. R., Blackford, M. G., Day, R. A. & Hart, K. P. The durability of synroc. *J. Nucl. Mater.* **190**, 287–294 (1992).
- Cao, C., Chong, S., Thirion, L., Mauro, J. C., McCloy, J. et al. Wet chemical synthesis of apatite-based waste forms—a novel room temperature method for immobilization of radioactive iodine. *J. Mater. Chem. A* **5**, 14331–14342 (2017).
- Redfern, S. A. T., Smith, S. E. & Maddrell, E. R. High-temperature breakdown of the synthetic iodine analogue of vanadinite, Pb-5(VO₄)(3): an apatite-related compound for iodine radioisotope immobilization? *Mineral. Mag.* **76**, 997–1003 (2012).
- Yao, T., Lu, F., Sun, H., Wang, J. & Ewing, R. C. et al. Bulk iodoapatite ceramic densified by spark plasma sintering with exceptional thermal stability. *J. Am. Ceram. Soc.* **97**, 2409–2412 (2014).
- Coulon, A., Grandjean, A., Laurencin, D., Jollivet, P. & Rossignol, S. et al. Durability testing of an iodate-substituted hydroxyapatite designed for the conditioning of I-129. *J. Nucl. Mater.* **484**, 324–331 (2017).
- Dorozhkin, S. V. A review on the dissolution models of calcium apatites. *Prog. Cryst. Growth Charact. Mater.* **44**, 45–61 (2002).
- Shimabayashi, S. & Matsumoto, M. Nonstoichiometric dissolution of hydroxyapatite in the presence of simple salts. *Nippon Kagaku Kaishi* **10**, 1118–1122 (1993).
- Oldfield, J. & Sutton, W. Crevice corrosion of stainless steels: i. a mathematical model. *Br. Corros. J.* **13**, 13–22 (1978).
- Oldfield, J. & Sutton, W. Crevice corrosion of stainless steels: II. Experimental studies. *Br. Corros. J.* **13**, 104–111 (1978).
- Glass, R. S., Overturf, G. E., Van Konynenburg, R. A. & McCright, R. D. Gamma radiation effects on corrosion—I. Electrochemical mechanisms for the aqueous corrosion processes of austenitic stainless steels relevant to nuclear waste disposal in tuff. *Corros. Sci.* **26**, 577–590 (1986).
- Farmer, J. & McCright, R. *General Corrosion and Localized Corrosion of Waste Package Outer Barrier*. No. ANL-EBS-MD-000003 (Yucca Mountain Project, 2000).
- He, X., Dunn, D. & Csontos, A. Corrosion of similar and dissimilar metal crevices in the engineered barrier system of a potential nuclear waste repository. *Electrochim. Acta* **52**, 7556–7569 (2007).
- Ikeda, B. & Quinn, M. *Corrosion of Dissimilar Metal Crevices in Simulated Concentrated Ground Water Solutions at Elevated Temperature*. No. AECL-12167 (Atomic Energy of Canada Limited, 2003).
- King, F. Container materials for the storage and disposal of nuclear waste. *Corrosion* **69**, 986–1011 (2013).
- Rebak, R. B. *Factors Affecting the Crevice Corrosion Susceptibility of Alloy 22*. No. UCRL-PROC-208265 (Lawrence Livermore National Lab (LLNL), Livermore, CA, 2004).
- Dunn, D., Pan, Y.-M., Chiang, K., Yang, L. & Cragolino, G. et al. The localized corrosion resistance and mechanical properties of alloy 22 waste package outer containers. *JOM* **57**, 49–55 (2005).
- Gordon, G. FN speller award lecture: corrosion considerations related to permanent disposal of high-level radioactive waste. *Corrosion* **58**, 811–825 (2002).
- Beavers, J., Devine Jr, T., Frankel, G., Jones, R., Kelly, R. et al. Peer review of the waste package material performance. *Final Report of the Waste Package Materials Performance Peer Review Panel* (2002).
- Shan, X. & Payer, J. Effect of polymer and ceramic crevice formers on the crevice corrosion of Ni-Cr-Mo alloy 22. *Corrosion* **66**, 105005–105005 (2010). -105014.
- Guo, X. et al. Self-accelerated corrosion of nuclear waste forms at material interfaces. *Nat. Mater.* <https://doi.org/10.1038/s41563-019-0579-x> (2020).
- Guo, X. W. et al. Corrosion interactions between stainless steel and lead Vanado-iodoapatite nuclear waste form—part I. Crevice corrosion of stainless Steel. *npj Mater. Degrad.* Submitted (2020).
- Rydborg, J. *Groundwater Chemistry of a Nuclear Waste Repository in Granite Bedrock*. No. UCRL-53155 (Lawrence Livermore National Lab, California, 1981).
- Fengyuan, L., Tiankai, Y., Yaron, D., Jianren, Z. & C. E. R. et al. Radiation stability of spark-plasma-sintered lead vanadate iodoapatite. *J. Am. Ceram. Soc.* **98**, 3361–3366 (2015).
- Wang, Y. Y. et al. Degradation mechanisms of lead-vanado-iodoapatite in liquid-mediated NaCl solutions. *Corros. Sci.* Submitted (2020).
- Sadat-Shojai, M., Khorasani, M.-T., Dinpanah-Khoshdargi, E. & Jamshidi, A. Synthesis methods for nanosized hydroxyapatite with diverse structures. *Acta Biomater.* **9**, 7591–7621 (2013).
- Pickering, H. & Frankenthal, R. On the mechanism of localized corrosion of iron and stainless steel I. Electrochemical studies. *J. Electrochem. Soc.* **119**, 1297–1304 (1972).
- Shojaei, E., Mirjalili, M. & Moayed, M. H. The influence of the crevice induced IR drop on polarization measurement of localized corrosion behavior of 316L stainless steel. *Corros. Sci.* **156**, 96–105 (2019).
- Zhang, Z., Gustin, L., Xie, W., Lian, J. & Valsaraj, K. T. et al. Effect of solution chemistry on the iodine release from iodoapatite in aqueous environments. *J. Nucl. Mater.* **525**, 161–170 (2019).
- Audubert, F., Carpena, J., Lacout, J. & Tetard, F. Elaboration of an iodine-bearing apatite iodine diffusion into a Pb3 (VO4) 2 matrix. *Solid State Ion.* **95**, 113–119 (1997).
- Kerrisk, J. F. *Groundwater Chemistry at Yucca Mountain, Nevada, and Vicinity*. No. LA-10929-MS (Los Alamos National Lab, 1987).
- Hem, J. D. *Study and Interpretation of the Chemical Characteristics of Natural Water* (Department of the Interior, US Geological Survey, 1985).
- Worthington, S., Marsh, G. & Taylor, K. Improvements in materials reliability in the back end of the nuclear fuel cycle. In Rojas, J. L. (ed.) *Proceedings of an IAEA Technical Committee Meeting, Vienna* (International Atomic Energy Agency, Austria) 55–64.
- Wronkiewicz, D. J., Bates, J. K., Wolf, S. F. & Buck, E. C. Ten-year results from unsaturated drip tests with UO₂ at 90 °C: implications for the corrosion of spent nuclear fuel. *J. Nucl. Mater.* **238**, 78–95 (1996).
- Cailleteau, C., Angeli, F., Devreux, F., Gin, S. & Jestin, J. et al. Insight into silicate-glass corrosion mechanisms. *Nat. Mater.* **7**, 978 (2008).
- Werme, L., Björner, I. K., Bart, G., Zwicky, H. U. & Grambow, B. et al. Chemical corrosion of highly radioactive borosilicate nuclear waste glass under simulated repository conditions. *J. Mater. Res.* **5**, 1130–1146 (1990).

ACKNOWLEDGEMENTS

This work was supported as part of the Center for Performance and Design of Nuclear Waste Forms and Containers, an Energy Frontier Research Center funded by the U.S. Department of Energy, Office of Science, Basic Energy Sciences under Award # DESC0016584.

AUTHOR CONTRIBUTIONS

T.K. and X.G. contributed equally to this study. T.K. and X.G. conceived the idea; T.K., X.G., P.L., and Y.W. conducted the experiments and analyzed the data; J.L. and G.S.F. supervised the study. All authors contributed to the editing of the paper, and approval of the content in its current form.

COMPETING INTERESTS

The authors declare no competing interests.

ADDITIONAL INFORMATION

Correspondence and requests for materials should be addressed to J.L.

Reprints and permission information is available at <http://www.nature.com/reprints>

Publisher's note Springer Nature remains neutral with regard to jurisdictional claims in published maps and institutional affiliations.



Open Access This article is licensed under a Creative Commons Attribution 4.0 International License, which permits use, sharing, adaptation, distribution and reproduction in any medium or format, as long as you give appropriate credit to the original author(s) and the source, provide a link to the Creative

Commons license, and indicate if changes were made. The images or other third party material in this article are included in the article's Creative Commons license, unless indicated otherwise in a credit line to the material. If material is not included in the article's Creative Commons license and your intended use is not permitted by statutory regulation or exceeds the permitted use, you will need to obtain permission directly from the copyright holder. To view a copy of this license, visit <http://creativecommons.org/licenses/by/4.0/>.

© The Author(s) 2020